Electrokinetic desalting and salting of water-in-oil droplets

Aparna Krishnamurthy and Robbyn K. Anand*

Department of Chemistry
Iowa State University
1605 Gilman Hall, 2415 Osborn Drive, Ames, IA, 50011, USA
*Corresponding author email: rkanand@iastate.edu

ABSTRACT: Droplet-based microfluidic platforms demand modifications to the droplet composition to facilitate reactions and analyses. However, limited techniques exist to modify the droplet contents post their generation. Here, ion transport across two ion-exchange membranes possessing distinct selectivity is employed to introduce ions into (salt) or extract ions from (desalt) water-in-oil droplets. The ion concentration distribution and transport mechanisms are visualized using a precipitation reaction and a charged fluorescent tracer. Further, current measurements reveal characteristic regimes in desalting and salting modes and demonstrate that the rates of ion transport linearly correlate with applied voltage and the ionic strength of the droplets. Importantly, up to 98% desalting efficiency is achieved. This technique advances droplet-based sample preparation through the straightforward manipulation of droplet contents.

Droplet microfluidics has profoundly advanced biotechnology and synthesis of particles. Many applications in these fields require the droplet contents to be manipulated either before or after droplet generation. For example, droplet-based mass spectrometry of bioanalytes may require the removal of unwanted salts from droplets while droplet-templated chemical or materials synthesis may require the addition of reagents into droplets. The manipulation of droplets is broadly relevant to many applications, such as for the synthesis of nanoparticles[1–4] and Janus particles[5,6], sample preparation[7,8], biochemical assays[9], and sensing[10,11]. Several passive and active strategies[12] or combinations thereof have been leveraged to manipulate droplet composition. Zaremba et al. used programmable syringe pumps and passive elements such as metering and merging traps to generate droplets with fixed or periodically distributed concentrations.[13] This concentration-on-demand platform provided control over the droplet composition, albeit with auxiliary steps involving volume addition (merging) or loss (splitting). Doonan and Bailey developed the K-channel which employs a cross-channel flow to the droplet flow, controlled by pressure and electric field for fluid extraction, reagent injection, and droplet splitting. The K-channel can be easily adapted to droplet microfluidic workflows and allows 0-100% volume changes.[14] Niu et al. developed a microdroplet dilutor for high-throughput screening that utilizes droplet merging, mixing, and re-splitting for controlling the droplet concentration.[15] In the droplet CAR-wash (coalesce-attract-re-segment) technique, developed by the Bailey group, the droplet media can be exchanged with the retention of encapsulated particles such as magnetic beads without compromising throughput.[16] The droplet CAR-wash technique is useful for on-chip buffer exchanges and rinsing – two steps that are extensively applied in biochemical assays involving the capture, modification, and analysis of solid particles. However, control over the extent of reagent (or buffer) exchange is limited in the droplet CAR-wash technique. Other methods to control the droplet composition include the use of valves and microfluidic analog-to-digital converters (μADCs).[12] However, in most of these systems, the point of manipulation is prior to or during droplet formation, with the droplet contents largely unchanged after generation. Although, electrocoalescence[17] and picoinjection[18,19] have been used for droplet manipulation post formation, their throughput and efficiency is limited by the number and placement of the electrical components. The discussed techniques in literature accomplish droplet manipulation to meet specific applications. However, few advancements have accomplished droplet manipulation without significantly altering the original droplet volumes or providing control over the amount of ions injected, exchanged, or removed.

To this end, ion-exchange membranes have been widely employed for controlling ion-transport and manipulating ionic strength in microscale systems. Microscale membrane-based ionic manipulation has been primarily achieved using dialysis, electrodialysis (ED), and ion concentration polarization (ICP).[20] ED uses an applied electric field to drive bipolar ion conduction across anion-exchange and cation-exchange membranes (AEM and CEM) resulting in concentrated and diluted streams of the sample. Kwak and coworkers first reported a microscale experimental model for ED and characterized the concentration profiles and associated electroconvection.[21] ICP, on the other hand, involves the electrokinetic transport of ions across a permselective membrane leading to the formation of ion depleted and enriched zones on opposing sides of the membrane. Serial arrangement of two membranes that are permselective for the same

charge of ionic species (e.g., two CEMs) will result in the formation of neighboring depleted and enriched zones thereby establishing a steep gradient in concentration. While ED and ICP are extensively researched topics, much of the work in these fields deals with samples which comprise a single phase, and little has been explored for bi- and multi-phasic samples such as droplets or other emulsions. Our group recently reported ICP within nanoliter-scale water-in-oil droplets.[10] Such in-droplet ICP was utilized to drive concentration enrichment and separation of charged molecules and to exchange the cationic content of the droplets.[10] However, ion exchange in the developed platform was limited by the monodirectional transport of predominantly one type of charged species (in this case, cations) across the droplets. In the context of ion-exchange, a platform that provides tunable transport of both cationic and anionic species is desirable for titrating, exchanging, or removing charged species.

Here, we report a technique called droplet ion manipulation and exchange (DIME) to accomplish net injection or removal of ions in the context of droplet microfluidics. This manipulation of droplet composition is accomplished through electrokinetically-driven ion transport across distinct ion-exchange membranes (AEM and CEM) contacting the droplets. Monitoring of each - the distribution of a fluorescent tracer and a model precipitation reaction reveals that ion transport in the developed system is directional (inward into the droplets with salting and outward with desalting), selective for the charge of ions, and occurs simultaneously across both the membranes. Measurement of current reveals distinct regimes in desalting and salting modes and in combination with fluorophore monitoring provides mechanistic insights on the observed trends in current. Based on these measurements, the applied voltage, and the relative ionic strengths of both the droplets and auxiliary channels were found to affect the rates of ion transport. Importantly, in-situ evaluation of droplet conductivity indicates over 97% desalting efficiency and the ability to reconcentrate the droplets to original concentration in the salting mode, accomplished within tens of seconds (few seconds in flowing droplets). These results demonstrate that the reported platform advances the toolkit available for droplet-based sample preparation by accessing on-demand, quantitative and selective ion extraction, ion injection, and ion exchange.

MATERIALS AND METHODS

Chemicals. The dianionic fluorophore (BODIPY^{2-} 4,4-difluoro-1,3,5,7,8-pentamethyl-4-bora-3a,4a-diaza-s-indacene-2,6-disulfonic acid) was obtained from Molecular Probes (Eugene, OR). The following reagent grade materials were used as received; Na_3PO_4, Na_2HPO_4, $AgNO_3$, $CaCl_2$. Nafion perfluorinated resin (20 wt% solution in lower aliphatic alcohols) was purchased from Sigma-Aldrich, (St. Louis, MO) and diluted with 200 proof ethanol (Fisher Scientific) in 1:3 ratio. Sustainion XA 9 ionomer solution in 5% ethanol was purchased from Dioxide Materials (Boca Raton, FL). All solutions were made in double deionized water (18.2 MΩ cm, Sartorius Arium Pro, Göttingen, Germany). Droplet (dispersed phase) compositions were distinct across different experiments and have been delineated under respective subsections. For the continuous phase, heavy mineral oil with 0.1 w/w% of Triton-X100 (Fisher bioreagents) and 3 w/w% of ABIL EM 90 (Evonik Industries, Essen, Germany) was used. Poly(dimethylsiloxane) (Sylgard 184 elastomer kit, Dow Corning Corp., Midland, MI) was used for device fabrication. Platinum wires (99.95%, 0.5 mm diameter) were purchased from Strem Chemicals (Newburyport, MA).

Device fabrication. A similar device fabrication protocol as our previous works was followed.[10,11] Briefly, standard soft lithography techniques were used to fabricate poly(dimethylsiloxane) (PDMS) devices. Microscope glass slides were cleaned in a base bath containing 1:1:1 solution of hydrogen peroxide, ammonium hydroxide and double deionized (DDI) water at 90 °C for 1 h. Then, the slides were rinsed with DDI water followed by rinsing with 200 proof ethanol, and dried using nitrogen gas. The PDMS chips with the design for the membranes were reversibly bonded over the clean glass slides. Nafion (1:3 in ethanol) and Sustainion solutions were separately flow-patterned along two parallel microchannels via capillary action. These slides were then subjected to soft baking at 65 °C for 30 min followed by heating at 95 °C for 10 min on a hot plate to completely cure the membranes. The reversibly bonded chips were then peeled off to reveal the membranes. A razor blade was used to cut off excess Nafion or Sustainion membranes, and ethanol was used to wipe away any residue. Next, the PDMS chips with the microchannel design and the glass slides with the patterned membranes were treated to air plasma (PDC-001, Harrick Plasma, Ithaca, NY) and irreversibly bonded to align the microchannel design over the patterned membranes. The assembled device was baked at 65 °C for more than 24 h to strengthen the bonding. Details of fabrication of gold microelectrodes and in-situ current measurements are provided later in the *Materials and methods section*. The device comprises a droplet generation zone in which channels leading from the inlet reservoirs of the aqueous (dispersed) and oil (continuous) phases converge at a T-junction to generate water-in-oil droplets. The aqueous and oil phases were dispensed at flow rates of 100 nL/min and 150 nL/min, respectively, using Pico Plus Elite syringe pumps (Harvard Apparatus, Holliston, MA) and 1 mL plastic syringes (Becton Dickinson and company, NJ) to generates water-in-oil droplets having volumes of 1.90 ± 0.05 nL.

Device dimensions. The critical geometric dimensions of each of the main channel and auxiliary channels are 250 μm wide and 41 μm tall. The distance between the main channel and each of the auxiliary channels is 150 μm. The AEM and CEM were 230 μm in width and 5-

10 µm in average thickness, measured using a profilometer (KLA Tencor™ Stylus, CA). The intermembrane spacing was 190 µm.

Imaging. Fluorescence and brightfield imaging were performed using an Eclipse Ti-S inverted fluorescence microscope (Nikon Industries, New York, NY) equipped with a digital camera (Orca Flash 4.0, Hamamatsu Corp., Bridgewater, NJ). Videos were recorded at a frame rate of 15 fps.

Data processing and analysis. MATLAB R2019b was used to plot the data for current measurements. ImageJ 1.53a software was used to process the images and videos. ImageJ was used to profile the fluorescence intensities.

Gold microelectrodes dimensions and fabrication. A pair of microelectrodes were each incorporated upstream and downstream of the EK zone for current measurements prior to and post desalting or salting (**Figure S17**). Each electrode in a pair was 40 µm wide and 40 µm apart from the other electrode. The gold microelectrodes were fabricated by standard photolithography and etching procedures. Briefly, gold-coated slides (EMF Corp., Ithaca, NY) were spin-coated with a positive photoresist AZ P4620 (Integrated Micro Materials (IMM), Argyle, TX). A mask comprising the electrode design was used to expose the slide to UV light at an intensity of 350 mJ/cm^2. After UV exposure, the slide was treated with an AZ 400 K developer (IMM, Alfa Aesar) for 5 min with agitation to remove the photoresist layer to reveal the gold electrodes. Then, the slide was rinsed with water and dried with nitrogen gas followed by treatment with a gold etchant solution (4% KI and 1% I_2) for ~35 s. The slide was then rinsed and dried again before treating with a chromium etchant solution (Sigma Aldrich, St. Louis, MO) for under 10 s. The above steps were performed to remove uncured photoresist and residual materials to leave behind the desired gold electrodes. The gold electrode slides were then treated with acetone (agitated for 5 min) and cleaned in a basebath containing 1:1:1 solution of hydrogen peroxide, ammonium hydroxide and double deionized (DDI) water at 90 °C for 1 h. Thereafter, the same fabrication procedure involving flow-patterning of membranes and irreversible bonding of PDMS microchannels onto the gold electrode slide was performed. Current measurements were made using a Keithley 2400 sourcemeter (Tektronix Inc., OR) and a Model 6487, Keithley Picoammeter (Tektronix Inc., Beaverton, OR).

Electrical setup for in-situ current measurements. The electrical setup involved connecting the device in series with a resistor of known resistance 1kΩ. An oscilloscope (BK Precision, CA) was connected to measure the voltage drop across the known resistor. Total R = R_1 + R_2. The maximum voltage is dropped across the device (R_1). AC voltage of V_{pp} = 10 V was applied using a Tektronix AFG3011C waveform generator (Tektronix Inc., Beaverton, OR) at 100 kHz.

RESULTS AND DISCUSSION

Device design and operation. The design of the DIME device is illustrated in **Scheme 1a**. Details of device fabrication and critical geometric dimensions of the device are provided in the **Supporting Information (SI)**. The upstream segment of the device comprises a T-junction that generates water-in-oil droplets having volumes of 1.90 ± 0.05 nL. These droplets were flowed into the main channel of the electrokinetic (EK) zone of the device. The flow was then stopped to make the droplets stationary. While the methods reported here do not require that the droplets be kept stationary, this condition aided in method development and characterization of ion transport. The EK zone contains a main channel at the center and two parallel auxiliary channels located on either side of the main channel. The main channel is flanked by an AEM (Sustainion) on one side and a parallel CEM (Nafion) on the opposing side. The AEM and CEM are patterned thin films that extend underneath the microchannel walls. A

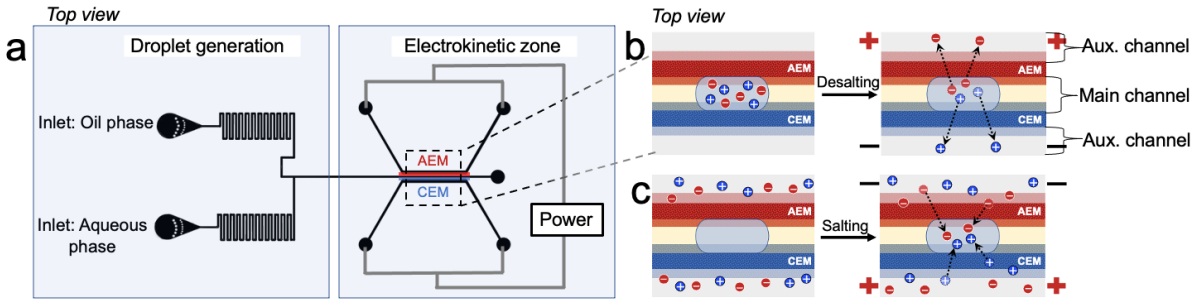

Scheme 1. (a) Schematic illustration of the device showing the droplet generation region and electrokinetic zone. Serpentine channels leading from the oil and aqueous phase inlet reservoirs converge at a T-junction to generate nanoliter-scale oil-in-water droplets. The electrokinetic zone comprises the AEM and CEM that connect parallel auxiliary channels to a central main channel into which the droplets are flowed. (b) Top view illustration showing the equilibrium distribution of ions within the droplet prior to desalting (left), and the extraction of ions from the droplet under an applied voltage in desalting mode (right). Note that to facilitate desalting, the AEM connects the anodic auxiliary channel to the droplet while the CEM connects the cathodic channel to the droplet. (c) Top view illustration showing the equilibrium distribution of ions in both the auxiliary channels prior to salting (left) and net movement of ions into the droplet in salting mode (right). In salting mode, the AEM connects the cathodic auxiliary channel to the droplet while the CEM connects the anodic auxiliary channel to the droplet.

schematic of the device fabrication procedure including patterning of the membranes is provided in the **SI (Figure S1)**.

The AEM and CEM contact the opposing ends of the droplets in the main channel and place them in ionic contact with the auxiliary channels, which are filled with an electrolyte solution. The reservoirs of the auxiliary channels contain driving electrodes (platinum wires) that are connected to a power supply. Under specific voltage and membrane configurations, ions were electrokinetically introduced into (salting) or extracted from (desalting) droplets. In desalting mode, the device was configured such that the CEM connected one side of the droplets to the cathodic auxiliary channel, while the AEM connected the opposing side of the droplets to the anodic auxiliary channel (**Scheme 1b**). On the other hand, in salting mode, the configuration was reversed, such that the anodic auxiliary channel contacted the droplets through the CEM, and the cathodic auxiliary channel through the AEM (**Scheme 1c**).

Evaluation of net ion movement via a model precipitation reaction. We investigated the net movement of ions into and out of the droplets under a voltage applied in the salting or desalting modes by leveraging AgCl precipitation as a model reaction that yields a visible product. The auxiliary channels were filled with 1.0 M $AgNO_3$ solution (pH 5.62, conductivity 71.99 mS/cm), and the droplets comprised 1.0 M $CaCl_2$ solution (pH 6.07, conductivity 121.9 mS/cm). Under specific voltage configurations, the location of AgCl precipitate indicated whether ions were injected into or extracted from the droplets.

In desalting mode **(Scheme 1b)**, under the application of 30 V DC, AgCl precipitated within 30 s at the interface between the AEM and the anodic auxiliary channel (**SI, Figure S2 and Movie S1**), with the amount of precipitate increasing over time. Some non-specific precipitation was observed on the CEM-droplet interface due to the diffusion-based interaction of in-droplet Cl^- with the $AgNO_3$-wetted CEM or possible device leakage.

The localization of the AgCl precipitation at the AEM-anodic channel interface is significant because it confirms that in desalting mode, ions migrate outward – Cl^- ions migrate out of the droplets, across the AEM, and towards the anodic auxiliary channel. Since the AEM was wetted by the $AgNO_3$ solution of the anodic auxiliary channel, AgCl precipitation occurs directly over the AEM-anodic channel interface. An additional feature of these results is that the AgCl precipitation was spatially dispersed, which makes the result less clear. This dispersion occurs because the Cl^- ions take many paths across the membrane.

Therefore, to further validate the direction of net ion movement, the device design was modified to include notches in the auxiliary channel walls (**Figure 1a**). These notches extend over the membranes and restrict the transport of ions to the exposed membrane segments. The model AgCl precipitation was carried out in this notched device. Upon the application of 30 V DC for 60 s to drive droplet desalting, AgCl precipitated within the notches of the anodic auxiliary channel that extended over the AEM (**Figure 1b and Movie S2**). In this result, all the notches contain precipitate because they are all in close proximity to a droplet. In contrast, when the droplets were spaced farther apart (~400-600 μm apart), no precipitate was observed in the notches that were farthest from the droplets because of the high resistance to ion migration over the intervening distance (**Figure S3**). Interestingly, the droplets were observed to deform and stretch under an applied voltage in desalting mode. This droplet stretching can be attributed to electrowetting. Further, over this 60 s of voltage application, a change in droplet volume is also observed. A key point is that this fluid transfer is co-directional with ion transport, which implies that it is attributable to electroosmotic withdrawal or addition of water from/to the droplets via the membranes. The dependence of the rate of this fluid transfer on controllable parameters is the subject of ongoing investigation in our laboratory.

In salting mode, under an applied voltage of 30 V DC, in-droplet AgCl precipitation was observed in a notched (**Figure 1c and Movie S3**) and an unnotched device (**Movie S4** and **Figure S4**). The precipitate forms at the anodic pole of the droplet, where Ag^+ ions enter via the CEM. This result is significant because it

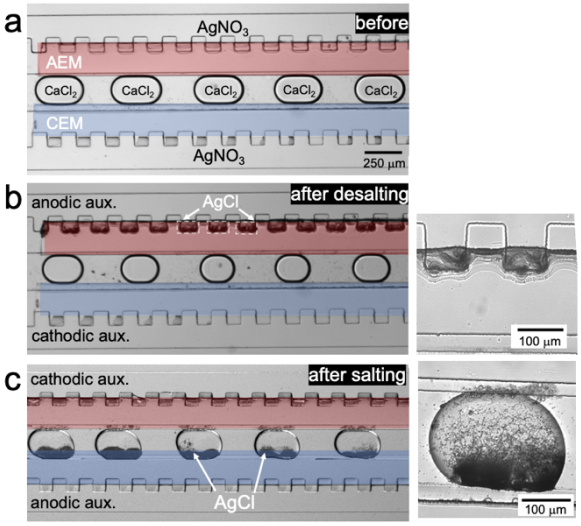

Figure 1. Brightfield micrographs showing - (a) the EK zone of a device containing $CaCl_2$ droplets in the main channel and notched auxiliary channels filled with $AgNO_3$, in the absence of an electric field. (b) AgCl precipitated on the notches of the anodic auxiliary channel following the application of 30 V DC for 60 s in desalting mode. Inset on the right shows the zoomed-in micrograph of the notches in the anodic auxiliary channel with AgCl precipitate. (c) In-droplet AgCl precipitation under an applied voltage of 30 V for 60 s in salting mode. Inset on the right shows a zoomed-in micrograph of in-droplet AgCl precipitation.

confirms the movement of ions into the droplet in salting mode.

In a set of control experiments, the compositions of the auxiliary channels and droplets were switched such that the droplets comprised 1.0 M $AgNO_3$ while the auxiliary channels were filled with 1.0 M $CaCl_2$. In desalting mode, AgCl precipitated at the CEM-cathodic auxiliary channel interface (instead of the AEM-anodic interface) because, in this configuration, Ag^+ (instead of Cl^-) migration out of the droplet drove precipitation (**Figure S5a**). In salting mode, AgCl precipitated within the droplet at the cathodic pole, where Cl^- ions entered (**Figure S5b**). The control experiments illustrate that injection or extraction of ions is not only directional (inward and outward) but also selective as governed by the permselectivity of the membranes employed.

To validate that ions are transported across both membranes at once, a separate experiment was performed. The droplets contained only 1.0 mM phosphate buffer while the auxiliary channel contacting the CEM was filled with 1.0 M $AgNO_3$, and the auxiliary channel that contacted the AEM was filled with 1.0 M $CaCl_2$. In salting mode under 30 V DC, AgCl precipitated within the droplet (**Movie S5** and **Figure S6a**). This result confirms the influx of Ag^+ and Cl^- ions through the CEM and AEM from respective auxiliary channels. In desalting mode, no precipitation was observed in this same system (**Figure S6b**).

Collectively, the results from the precipitation experiments indicate that the direction of net ion movement across the system is controlled by the electrophoretic movement of ions and the permselectivity of the membranes. These results also suggest a potential application of DIME for the introduction of salts to droplets at a controlled rate to guide crystallization. The operation of DIME is dependent on the wetting of the ion exchange membranes by the aqueous droplets, which establishes an ionic communication at the membrane-droplet interfaces for selective ion transport. Therefore, droplets must span the entire intermembrane gap, physically contacting the membranes on both sides. An interesting topic for further study would be to investigate how the cross-sectional overlap between the droplets and the membranes affects the efficiencies of ion extraction or injection.

Characterization of ionic distribution using fluorophore tracking. Next, we characterized the redistribution of ions within the droplets under desalting and salting conditions. Droplets comprising 10.0 µM of a dianionic fluorophore - BODIPY FL in 10.0 mM sodium phosphate buffer (PB) (pH 7.52, conductivity 595 µS/cm) were generated and stationed in the EK zone. In the absence of any electric field, the fluorophore was uniformly distributed across each droplet (**Figure 2a (top) and 2b (top);** plateaued shape of the inset plot showing intensity profile). Under 15 V DC (applied in a polarity appropriate for desalting), darkened regions and electroconvective vortices were observed on both the opposing membrane-droplet interfaces (**Figure 2a (middle);** bell-shaped intensity plot as inset). These observations are consistent with ion depletion from both the hemispheres of the droplet - at the AEM, the dye and anions of the electrolyte were extracted, while at the CEM, cations were extracted, and in their absence, the anionic dye was excluded from this region to maintain electroneutrality. Steep concentration and electric field gradients arising from ion depletion are known to drive electroconvection, which expedites ion transport to the membranes. Within 20 s, the droplet was no longer fluorescent, which indicates that the fluorophore was completely depleted (**Figure 2a (bottom)**).

Upon the application of 15 V DC in the reverse configuration (salting mode), an in-droplet concentration redistribution of the fluorophore was observed (**Figure 2b (middle)**). The anionic fluorophore migrated towards the anodic droplet hemisphere (contacting the CEM) leading to a local increase in concentration of about 20%. Further, no electroconvective vortices were observed with droplet salting. The redistribution of the anionic fluorophore indicates that under an applied voltage for droplet salting, the negatively charged dye present within the

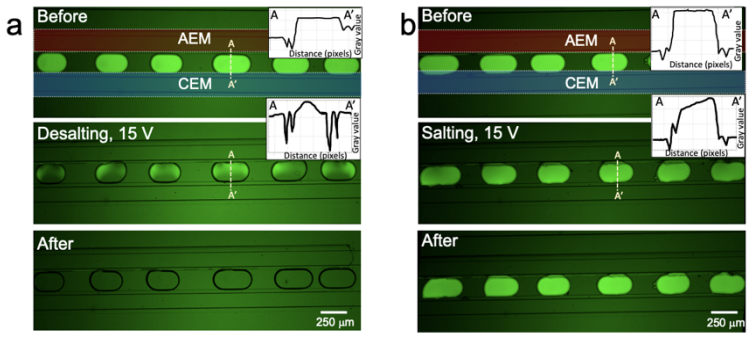

Figure 2. Green fluorescence micrographs showing - (a) fluorophore distribution in droplets before voltage application (top), fluorophore depletion at opposing droplet hemispheres (center), and negligible in-droplet fluorescence after the application of 15 V for 20 s (bottom), in desalting mode. (b) Fluorophore distribution within droplets before (top), during (middle), and after (bottom) voltage application (top), in salting mode. Insets show the concentration distribution of the fluorophore across the dashed lines labelled A-A'.

droplet migrates towards the anodic hemisphere of the droplet and charge pairs with cations entering via the CEM. It should be noted however, that the CEM restricts the outward movement of the anionic species thereby trapping it within the droplet. This result is important because it illustrates that "salting mode" is a method to introduce ionic species into the droplet without allowing existing encapsulated charged species to escape. After the voltage is switched off, the droplets regain uniform fluorophore distribution (**Figure 2b (bottom)**).

Next, we completely filled both the auxiliary channels and the main channel with this fluorophore solution (as a single phase) to evaluate the role of the auxiliary channels as ion sources or sinks by monitoring the dye distribution. In desalting mode, the main channel was depleted of the fluorophore from either side with the dramatic formation of vortices under 50 V DC (**Movie S6**). Under the applied voltage, the anionic dye in the cathodic auxiliary channel migrated away from the reservoirs and accumulated at the CEM-channel interface. The fluorophore in the anodic auxiliary channel invariably adsorbed onto the AEM nonspecifically while maintaining a uniform distribution in that channel. Similar fluorophore redistribution occurred when the main channel contained droplets instead of a single aqueous phase (**Figure S7** (desalting) and **Figure S8** (salting)). These results demonstrate that the auxiliary channels provide ions for salting or accumulate desalted ions based on the mode of operation.

Ion transport in the DIME technique is dependent on the relative sizes of the charged analyte and the pores on the ion exchange membranes. **Figure S9** compares the desalting responses of analytes of distinct sizes. Smaller analytes such as BODIPY FL are completely depleted from the droplet in the desalting mode. However, larger analytes such as proteins (for example, Texas red dye-conjugated bovine serum albumin (BSA)), antibodies (for example, Alexa Fluor 488-conjugated rabbit IgG), and microparticles (such as, polystyrene beads) are mostly retained, with some non-specific adsorption of analytes on the membranes.

Further, it was observed that ion depleted zones (IDZs) are generated with both droplet salting and desalting. These IDZs appear as darkened regions depleted of the charged fluorophore either within the auxiliary channels or the droplets. With droplet desalting, the IDZs appear on opposing hemispheres of a droplet contacting the membranes, while in salting mode, the IDZs form along the auxiliary channel-membrane interfaces. IDZs are problematic because they suppress further electrokinetically-driven mass transport and therefore, limit the efficiency of salting or desalting. To improve mass transport, the concentration gradients generated in the system under the applied voltage need to be quelled. Kim and coworkers incorporated microstructures (cylindrical posts) that redistributed the local flow velocities near the AEM and CEM of a model ED system and therefore, enhanced mass transport.[22] Jang et al. investigated the use of partially masked ion exchange membranes to improve ion transport and current efficiencies in microfluidic electrodialysis.[23] They reported that masking opposing AEM and CEM parallelly with shorter masked and unmasked unit lengths improved current densities and enhanced ion transport. Such strategies leverage the device design to enable mixing and ion redistribution.

In a simplistic approach not requiring any device re-engineering, we investigated the rate of desalting via current measurements made under conditions of droplet flow. The desalting of flowing droplets was studied rather than salting because in-droplet fluorophore depletion is a straightforward visual endpoint for desalting. Droplets comprising 10.0 μM BODIPY FL in 10.0 mM PB (pH 7.52, conductivity 595 μS/cm) were generated and flowed into the device at a rate of 0.15 mm/s (oil phase flow rate = 150 nL/min, dispersed phase flow rate = 100 nL/min). **Movie S7** shows fluorophore depletion in flowing droplets spiked with BODIPY FL under a continuous application of 30 V for desalting. A flowing droplet was depleted of the fluorophore completely within 2-3 s of entering the EK zone (**Movie S7**). On the other hand, complete fluorophore depletion at 30 V for a stationary set of droplets took nearly 10 s – nearly an order of magnitude longer. Flowing droplets possess internal counter-rotating recirculation zones.[24,25] Under an applied voltage for desalting or salting, flowing droplets experience the perturbation of IDZs by this recirculation. Convective flow of droplets enables in-droplet mixing and improves ion conductivity and therefore, ion transport. As indicated by the fluorophore tracking studies, the rate of desalting is higher in flowing droplets compared to stationery droplets. This result provides a scope for investigating the effect of flow rates on desalting efficiencies. It is anticipated that the rate of ion transport improves with flow rates. However, very high flow rates would likely disrupt DIME operation due to the insufficient time for the electrokinetic transport of ions across droplet boundaries. This issue could be addressed with a longer EK zone.

The rate of ion exchange is also voltage dependent. **Movies S7-S9** are fluorescence video micrographs of flowing droplets experiencing desalting under 30 V, 15 V, and 7.5 V, respectively. The rate of fluorophore depletion was directly dependent on applied voltage at this set flow rate. Therefore, the fluorophore was depleted fastest at 30 V compared to 7.5 V. **Movies S10-S12** are fluorescence video micrographs of flowing droplets undergoing salting at voltages of 30 V, 15 V, and 7.5 V. With salting, the flowing droplets exhibit redistributed concentrations of the dye, which is spatially confined at the anodic hemisphere until the droplets leave the EK zone. The concentration gradient was steepest at 30 V and most diffuse at 7.5 V.

These fluorophore tracking experiments enabled the real-time visualization of the net movement and distribution of ions across the entire EK zone. The auxiliary channels and the droplets act either as sources or sinks for ions based on the mode of operation (salting or desalting). Ion transport in the developed platform is selective for the size and the charge of the analyte and depends on the pore sizes of the membranes and their charge permeability. A very small fluorophore like BODIPY FL is readily extracted and also adsorbed onto the AEM. However, in salting mode, the BODIPY FL is entrapped within the droplet because of the permselectivity of the CEM which restricts outward mass transport of the anionic fluorophore. Thus, with the exception of any diffusion-based partitioning of species between the oil and aqueous phases, the injection or extraction of ions by DIME is strictly electrokinetic. In the context of sample preparation, this is a significant advancement because it provides on-demand control over the droplet composition.

Current measurement to determine rates of ion transport. We characterized current transients obtained for a stationary set of droplets in the EK zone under droplet desalting and salting conditions. In both salting and desalting modes, a voltage bias of 30 V DC was applied for 60 s across the EK zone that contained around five to seven stationary droplets in the main channel and the current transients over the duration of voltage application were measured using a 2450 Keithley source meter. The droplets and auxiliary channels both comprised 10.0 mM PB (pH 7.52, 595 µS/cm). Under droplet desalting conditions, an initially high current (several µA), gradually decreased over time to several nA, exhibiting a characteristic three-regime sigmoidal trace as shown in **Figure 3a**. The first regime denotes the onset of desalting such that an initially high current begins decreasing over the first few seconds (0-5 s) of voltage application. The higher initial current is attributed to the ohmic resistance of the electrolyte and membranes at the initial ionic distribution across the EK zone including that within the droplets. As desalting proceeds, the current decreases gradually and then drops steeply (slope on the order of 10^{-7} A over 5 s (between 5-10 s)) denoting decreased ion transport in the second regime. This steep negative gradient in current can be attributed to the formation of highly resistive IDZs. Finally, the current plateaus to a low value (tens of nA) indicating negligible ionic strength of the desalted droplets that act as 'open' switches and break the ionic circuit across the EK zone. The rate of desalting is linearly proportional to the current and decreases over time as the droplets are continuously depleted of ions. Additionally, the area under the *i-t* plot provides an estimate of the amount of charge depleted from a set of droplets.

In salting mode (**Figure 3b**), it can be observed that the current gradually and linearly ($R^2 = 0.97 \pm 0.02$, $n = 3$ trials - in the same device with a new set of droplets each time) decreases over time. However, this gradual decrease in current with droplet salting does not correlate with the droplet's conductivity. Instead, the decrease in current with droplet salting is attributed to the formation of IDZs at both the membrane-auxiliary channel interfaces. Therefore, the rate and efficiency of salting cannot be estimated from the *i-t* trace. To address this issue, we developed an electrical setup to determine the absolute change in a droplet's ionic current, which is reported in the last subsection.

To determine the effect of applied voltage on the rates of desalting and salting, current was measured under distinct applied voltages. The characteristic trends in current transients for desalting and salting were obtained under distinct voltages, with the initial rates of desalting and salting being linearly proportional to the applied voltage. Details are provided in SI text and **Figures S10 and S11**. The current transients for continuously flowing droplets were also monitored (SI text and **Figures S12-S14**) and followed a periodic trend, while a single flowing droplet followed a bell-shaped (desalting mode) or plateaued (salting) trend.

Collectively, results from the current measurements indicate – (1) characteristic regimes in current transients obtained in desalting and salting modes, and

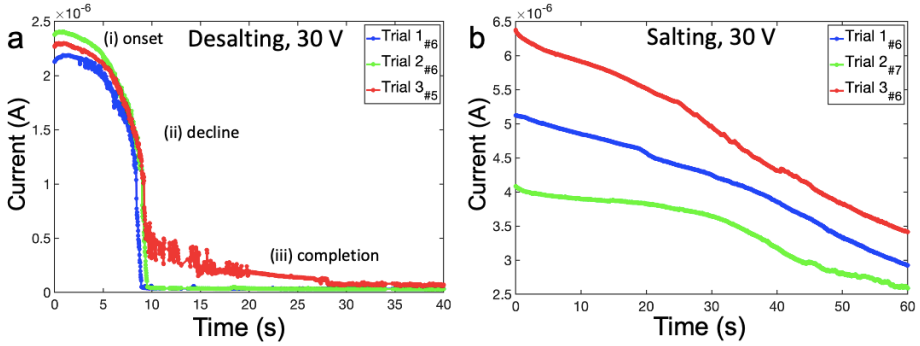

Figure 3. Current transients for a stationary set of droplets (~2 nL each) undergoing (a) desalting at 30 V for three distinct trials each with five or six droplets in the EK zone as indicated in the key ; the characteristic three-regime trace depicts the onset, decline, and completion of desalting. (b) Salting at 30 V over three trials with six or seven droplets in the EK zone; the current decreases over time due to the formation of IDZs in the auxiliary channel interfaces. Droplets and auxiliary channels comprise 10.0 mM PB.

(2) linear correlation between the rates of ion transport and the applied voltage, and inverse proportionality between the applied voltage and time to accomplish complete desalting (minima in *i-t* plot), These results are important as they can be leveraged to optimize the magnitude and duration of applied voltage for precise control over the amount of ions transported.

Finally, to evaluate the effect of ionic strength of the droplets and auxiliary channels on the rates of each desalting and salting, their compositions were varied. These experiments and the results (**Figure S15** and **S16**) are discussed in the SI. Briefly, these results indicate that in the present device configuration, there is a similar magnitude impact of droplet and auxiliary channel composition on the overall resistance of the EK zone and that the desalting and salting rates are dictated by the formation of IDZs, which take longer to form in droplets with higher ionic strength. The current reflects ion distribution, rather than the extent of desalting or salting. This limitation necessitates the direct measurement of droplet conductivity – this need is addressed next.

Efficiency of desalting. In the preceding subsections, the reported current depended on contributions to impedance from all components of the EK zone - auxiliary channels, droplets, and membranes. A method that determines the conductivity of the droplets alone (in the absence of IDZs) is required to evaluate the efficiency of desalting and the capability to reconcentrate the droplets. To this end, we incorporated gold microelectrodes into the device for in-situ conductivity measurements. Details of the fabrication protocol, electrical setup and measurement technique are provided in the **SI, Figure S17**. Briefly, the auxiliary channels comprised 10.0 mM PB. Before desalting, each droplet (100.0 mM PB) was positioned right above the upstream pair of microelectrodes, and the voltage dropped across the known resistor was measured using an oscilloscope. Following this, the droplets were pushed into the EK zone where they were desalted. Finally, these droplets were flowed further downstream, and each droplet was positioned over the second set of electrodes for the voltage drop to be measured. Subsequently, the current associated with each droplet was calculated from the measured voltage drop. This same set of droplets (that were desalted), were then salted and the current measurement repeated.

The results obtained are reported in **Table 1**. The efficiency of desalting was calculated as:

$$Eff_{desalting} = \frac{(i_i - i_f)}{i_i} \times 100$$

$$= \frac{(537.33 - 11.2)}{537.33} \times 100 = 97.9\%$$

Where i_i is the initial value of current across the droplet prior to its desalting and i_f is the final value of current measured across the droplet after desalting upon applying 30 V DC for 60 s. Current measurements from salting the same set of desalted droplets indicate that the concentration of desalted droplets reverts to the original concentration under identical experimental conditions of applied voltage and time in the salting mode. Further, a calibration plot comparing the ionic current corresponding to droplets comprising distinct concentrations of PB (**Table S1** and **Figure S18)** was obtained. From the calibration plot, it can be observed that when droplets comprising 100.0 mM PB are desalted under 30 V for 60 s, the final current corresponds to that for a 1.0 mM droplet, therefore, nearly 100-fold dilution of the droplets is achieved.

CONCLUSION

The developed droplet microfluidic technique - DIME, incorporates two distinct ion exchange membranes and electrokinetically drives the selective extraction of ions from or introduction of ions into water-in-oil droplets. Droplet desalting and salting are visually demonstrated through both the localization of precipitation reactions and the redistributions of a fluorescent tracer. Current transients quantify the rate of ion transport and reveal distinct regimes in desalting and salting modes driven by localized formation of highly resistive IDZs.

Table 1: Values of measured voltage and calculated current for - (a) three droplets comprising 100 mM sodium phosphate buffer that were desalted by applying 30 V for 60 s, (b) three droplets that underwent desalting and were then salted by applying 30 V for 60 s.

	Voltage (mV)							
Desalting	D1	D2	D3	Mean	StDev	Current (μA)	StDev	Desalting efficiency
Before	412	440	760	537.33	193.34	537.33	0.00019	97.915
After	11.6	10.8	11.2	11.2	0.4	11.2	4E-07	
	Voltage (mV)							
Salting	D 1	D2	D3	Mean	StDev	Current (μA)	StDev	
Before	11.6	10.8	11.2	11.2	0.4	11.2	4E-07	
After	432	400	444	425.33	22.744	425.333	2E-05	

Further, the dependence of the rate of ion transport on the applied voltage, ionic strength, and capacitive charging is characterized. A key result is that the rate of droplet desalting is increased by nearly an order of magnitude by flowing the droplets along the microchannel to induce convective mixing – a strategy important for practical application of this method. Importantly, over 97% desalting efficiency is achieved with the capability to reconcentrate the droplets back to original concentrations by using the salting mode to reintroduce salts into the droplet. The developed platform significantly adds to the droplet-based sample preparation toolkit by providing control over functions such as selective injection and extraction of charged species, or their exchange.

Currently, there are limited techniques to manipulate the droplet contents post their generation. Specifically, in-line droplet manipulation is required to bypass intervening steps in sample preparation including solution exchanges, reagent addition, or removal of interferents. Our technique accomplishes these functions and is especially relevant to droplet-based mass spectrometric bioanalysis. For example, desalting can be leveraged to suppress matrix interference by removing adduct-forming ions from droplets that comprise bioanalytes. Droplet salting on the other hand, can be used for analyte derivatization for mass spectrometry. Like in other membrane-based analytical techniques, we anticipate challenges such as membrane fouling by the droplet contents, leaking of stray ions across membranes, and chemical or biological incompatibility between membranes and the droplet contents. However, these limitations can be addressed by employing customized membrane materials or surface-coating strategies. For droplets encapsulating bioanalytes, pH shifts in response to ICP at the respective membranes may also pose a challenge. These aspects of DIME are the focus of ongoing research in our group.

ASSOCIATED CONTENT

Supporting Information

The Supporting Information is available free of charge on the ACS Publications website.

Additional experimental details on the effect of ionic strength on the rates of desalting and salting (text). Detailed device fabrication procedure (**Figure S1**), brightfield micrographs showing location of model precipitation under distinct compositions of droplets and auxiliary channels (**Figures S2-S6**). Green fluorescence micrographs showing distribution of model analyte BODIPY FL, under desalting (**Figure S7**) and salting (**Figure S8**) conditions. Distribution of analytes with distinct sizes under desalting mode (**Figure S9**). Current transients at distinct voltages in desalting (**Figure S10**) and salting (**Figure S11**) modes. Current transients obtained in desalting (**Figure S12**) and salting (**Figure S13**) modes for continuously flowing droplets at distinct applied voltages. Current transients obtained for a single flowing droplet in both modes (**Figure S14**). Current transients under distinct compositions of droplets and auxiliary channels to test effect of ionic strength for desalting (**Figure S15**) and salting (**Figure S16**). Circuit and electrical setup for in situ current measurements (**Figure S17**). Calibration plot for current versus droplet concentration (**Figure S18**). Values of measured voltage and calculated current for - droplets that were desalted or salted (**Table 1**) and droplets comprising distinct buffer concentrations (**Table S1**). Movie files showing model precipitation in the desalting mode in a normal (**Movie S1**) and notched (**Movie S2**) devices; salting in normal (**Movie S3**) and notched (**Movie S4**) devices. In-droplet salting when reagents start at opposite auxiliary channels (**Movie S5**). Green fluorescence video-graphs depicting analyte distribution in desalting (single phase at 50 V: **Movie S6**, with flow at distinct voltages: **Movie S7-S9**) and salting (with flow at distinct voltages: **Movie S10-S12**) modes.

ACKNOWLEDGEMENT

The authors gratefully acknowledge financial support for this research from an NSF CAREER grant awarded by the Chemistry Directorate, Chemical Measurement, and Imaging Program under award number 1849109. The authors thank group member Zisun Ahmed for help with constructing the electrical setup for in-situ current measurements.

AUTHOR INFORMATION

Corresponding Author

*Robbyn K. Anand − *Department of Chemistry, Iowa State University, Ames, Iowa 50011-1021, United States;*orcid.org/0000-0003-2801-8280;
Email: rkanand@iastate.edu

Author

Aparna Krishnamurthy − *Department of Chemistry, Iowa State University, Ames, Iowa 50011-1021, United States;* orcid.org/0000-0003-1123-1026

CONFLICT OF INTEREST

The authors declare no conflict of interest.

REFERENCES

(1) Ma, J.; Lee, S. M.-Y.; Yi, C.; Li, C.-W. Controllable Synthesis of Functional Nanoparticles by Microfluidic Platforms for Biomedical Applications – a Review. *Lab Chip* **2017**, *17* (2), 209–226. https://doi.org/10.1039/C6LC01049K.

(2) Gaikwad, G.; Bangde, P.; Rane, K.; Stenberg, J.; Borde, L.; Bhagwat, S.; Dandekar, P.; Jain, R. Continuous Production and Separation of New Biocompatible Palladium Nanoparticles Using a Droplet Microreactor. *Microfluid Nanofluidics* **2021**, *25* (3), 27. https://doi.org/10.1007/s10404-020-02410-x.

(3) Wang, J.; Li, Y.; Wang, X.; Wang, J.; Tian, H.; Zhao, P.; Tian, Y.; Gu, Y.; Wang, L.; Wang, C.

Droplet Microfluidics for the Production of Microparticles and Nanoparticles. *Micromachines (Basel)* **2017**, *8* (1). https://doi.org/10.3390/mi8010022.

(4) Bandulasena, M. V.; Vladisavljević, G. T.; Benyahia, B. Droplet-Based Microfluidic Method for Robust Preparation of Gold Nanoparticles in Axisymmetric Flow Focusing Device. *Chem Eng Sci* **2019**, *195*, 657–664. https://doi.org/10.1016/j.ces.2018.10.010.

(5) Liu, Y.; Nisisako, T. Microfluidic Generation of Monodispersed Janus Alginate Hydrogel Microparticles Using Water-in-Oil Emulsion Reactant. *Biomicrofluidics* **2022**, *16* (2), 024101. https://doi.org/10.1063/5.0077916.

(6) Nie, Z.; Li, W.; Seo, M.; Xu, S.; Kumacheva, E. Janus and Ternary Particles Generated by Microfluidic Synthesis: Design, Synthesis, and Self-Assembly. *J Am Chem Soc* **2006**, *128* (29), 9408–9412. https://doi.org/10.1021/ja060882n.

(7) Papadimitriou, V. A.; Kruit, S. A.; Segerink, L. I.; Eijkel, J. C. T. Droplet Encapsulation of Electrokinetically-Focused Analytes without Loss of Resolution. *Lab Chip* **2020**, *20* (12), 2209–2217. https://doi.org/10.1039/D0LC00191K.

(8) Saucedo-Espinosa, M. A.; Dittrich, P. S. In-Droplet Electrophoretic Separation and Enrichment of Biomolecules. *Anal Chem* **2020**, *92* (12), 8414–8421. https://doi.org/10.1021/acs.analchem.0c01044.

(9) Kaminski, T. S.; Garstecki, P. Controlled Droplet Microfluidic Systems for Multistep Chemical and Biological Assays. *Chem Soc Rev* **2017**, *46* (20), 6210–6226. https://doi.org/10.1039/C5CS00717H.

(10) Kim, S.; Ganapathysubramanian, B.; Anand, R. K. Concentration Enrichment, Separation, and Cation Exchange in Nanoliter-Scale Water-in-Oil Droplets. *J Am Chem Soc* **2020**, *142* (6), 3196–3204. https://doi.org/10.1021/jacs.9b13268.

(11) Kim, S.; Krishnamurthy, A.; Kasiviswanathan, P.; Ganapathysubramanian, B.; Anand, R. K. In-Droplet Electromechanical Cell Lysis and Enhanced Enzymatic Assay Driven by Ion Concentration Polarization. *Anal Chem* **2023**, *95* (39), 14624–14633. https://doi.org/10.1021/acs.analchem.3c02414.

(12) Shi, N.; Mohibullah, M.; Easley, C. J. Active Flow Control and Dynamic Analysis in Droplet Microfluidics. *Annual Review of Analytical Chemistry* **2021**, *14* (1), 133–153. https://doi.org/10.1146/annurev-anchem-122120-042627.

(13) Zaremba, D.; Blonski, S.; Korczyk, P. M. Concentration on Demand – A Microfluidic System for Precise Adjustment of the Content of Single Droplets. *Chemical Engineering Journal* **2022**, *430* (October 2021), 132935. https://doi.org/10.1016/j.cej.2021.132935.

(14) Doonan, S. R.; Bailey, R. C. K-Channel: A Multifunctional Architecture for Dynamically Reconfigurable Sample Processing in Droplet Microfluidics. *Anal Chem* **2017**, *89* (7), 4091–4099. https://doi.org/10.1021/acs.analchem.6b05041.

(15) Niu, X.; Gielen, F.; Edel, J. B.; DeMello, A. J. A Microdroplet Dilutor for High-Throughput Screening. *Nat Chem* **2011**, *3* (6), 437–442. https://doi.org/10.1038/nchem.1046.

(16) Doonan, S. R.; Lin, M.; Bailey, R. C. Droplet CAR-Wash: Continuous Picoliter-Scale Immunocapture and Washing. *Lab Chip* **2019**, *19* (9), 1589–1598. https://doi.org/10.1039/C9LC00125E.

(17) Bhattacharjee, B.; Vanapalli, S. A. Electrocoalescence Based Serial Dilution of Microfluidic Droplets. *Biomicrofluidics* **2014**, *8* (4), 044111. https://doi.org/10.1063/1.4891775.

(18) Abalde-Cela, S.; Taladriz-Blanco, P.; De Oliveira, M. G.; Abell, C. Droplet Microfluidics for the Highly Controlled Synthesis of Branched Gold Nanoparticles. *Sci Rep* **2018**, *8* (1), 1–6. https://doi.org/10.1038/s41598-018-20754-x.

(19) Abate, A. R.; Hung, T.; Mary, P.; Agresti, J. J.; Weitz, D. A. High-Throughput Injection with Microfluidics Using Picoinjectors. *Proceedings of the National Academy of Sciences* **2010**, *107* (45), 19163–19166. https://doi.org/10.1073/pnas.1006888107.

(20) Roelofs, S. H.; van den Berg, A.; Odijk, M. Microfluidic Desalination Techniques and Their Potential Applications. *Lab Chip* **2015**, *15* (17), 3428–3438. https://doi.org/10.1039/C5LC00481K.

(21) Kwak, R.; Guan, G.; Peng, W. K.; Han, J. Microscale Electrodialysis: Concentration Profiling and Vortex Visualization. *Desalination* **2013**, *308*, 138–146. https://doi.org/10.1016/j.desal.2012.07.017.

(22) Kim, B.; Choi, S.; Pham, V. S.; Kwak, R.; Han, J. Energy Efficiency Enhancement of Electromembrane Desalination Systems by Local Flow Redistribution Optimized for the Asymmetry of Cation/Anion Diffusivity. *J Memb Sci* **2017**, *524* (November 2016), 280–287. https://doi.org/10.1016/j.memsci.2016.11.046.

(23) Kim, M.; Kim, B. Study on Ion Transport and Electroconvection for Partially Masked Ion Exchange Membrane in Microfluidic

Electrodialysis. *Transactions of the Korean Society of Mechanical Engineers - B* **2022**, *46* (3), 133–140. https://doi.org/10.3795/KSME-B.2022.46.3.133.

(24) Hodges, S. R.; Jensen, O. E.; Rallison, J. M. The Motion of a Viscous Drop through a Cylindrical Tube. *J Fluid Mech* **2004**, *501*, 279–301. https://doi.org/10.1017/S0022112003007213.

(25) Baroud, C. N.; Gallaire, F.; Dangla, R. Dynamics of Microfluidic Droplets. *Lab Chip* **2010**, *10* (16), 2032. https://doi.org/10.1039/c001191f.

For Table of Contents Only